Numerical simulations of driven vortex systems

G. W. Crabtree, D. O. Gunter, H. G. Kaper, A. E. Koshelev, G. K. Leaf, and V. M. Vinokur
Argonne National Laboratory, Argonne, Illinois 60439
(Received 12 August 1999)

This paper reports on several large-scale numerical simulations of vortex systems that are driven through superconducting media with defects. The simulations are based on the time-dependent Ginzburg-Landau equations. The simulations demonstrate regimes of plastic and elastic steady-state motion in the presence of a twin boundary, show the effect of regular and irregular arrays of point defects on vortex trajectories, and show a mechanism by which vortices move through an array of columnar defects. Also presented are the results of some transient simulations in two and three dimensions, which show that, in the transition from the Meissner state to the vortex state, vortices are formed by a process of deposition.

I. INTRODUCTION

The quantitative exploration of the dynamic states of a vortex system driven through a superconducting medium poses formidable challenges, especially when there is a significant degree of disorder in the medium. Energy losses are inherent; hence, the definition of a free energy is ruled out, and the usual relations of thermodynamics do not apply. In cases like these, numerical simulations can yield information that is difficult or even impossible to obtain otherwise. In this article we report on several large-scale simulations of vortex systems that are driven through superconductor configurations with defects. We demonstrate regimes of plastic and elastic steady-state motion in the presence of a twin boundary, show the effect of regular and irregular arrays of point defects on vortex trajectories, and show a mechanism by which vortices move through an array of columnar defects. We also present the results of some transient simulations in two and three dimensions, which show that, in the transition from the Meissner state to the vortex state, vortices are formed by a process of deposition.

The simulations are based on the time-dependent Ginzburg-Landau (TDGL) equations.[1] The equations describe the state of a superconducting medium in terms of an order parameter and a vector potential. There are no assumptions about the number of vortices in the system or the vortex interaction laws. In this sense, the TDGL equations are more reliable than the equations of molecular dynamics, especially in cases where boundaries and nucleation processes are involved.

The numerical integration of the TDGL equations requires, however, considerable computational resources. The large-scale simulations reported here were carried out on the IBM SP system at Argonne and took typically on the order of hundreds of hours of CPU time. But, as our simulations demonstrate, realistic configurations can be modeled quite successfully, and significant results can be obtained.

The Ginzburg-Landau model of superconductivity and details of the numerical approximation are presented in Sec. II. Section III is devoted to simulations of driven vortex systems in the presence of a twin boundary (Sec. III A), point defects (Sec. III B), and columnar defects (Sec. III C). Section IV gives the results of some transient simulations illustrating the transition from the Meissner state to the vortex state in two and three dimensions. The results are summarized and discussed in Sec. V.

II. GINZBURG-LANDAU MODEL

The simulations described in this article are based on the macroscopic Ginzburg-Landau model of superconductivity.[1] They require the solution of two coupled partial differential equations for the complex-valued *order parameter* $\psi = |\psi| e^{i\phi}$ and the real vector-valued *vector potential* A,

$$\frac{\hbar^2}{2m_s D}\left(\frac{\partial}{\partial t}+\frac{ie_s}{\hbar}\Phi\right)\psi = -\frac{1}{2m_s}\left(\frac{\hbar}{i}\nabla-\frac{e_s}{c}\mathbf{A}\right)^2\psi + a\psi - b|\psi|^2\psi, \tag{1}$$

$$\nu\left(\frac{1}{c}\frac{\partial \mathbf{A}}{\partial t}+\nabla\Phi\right) = -\frac{c}{4\pi}\nabla\times\nabla\times\mathbf{A}+\mathbf{J}_s. \tag{2}$$

Here, Φ is the real scalar-valued *electric potential*, and $\mathbf{J}_s$ is the *supercurrent density*, which is a nonlinear function of ψ and $\mathbf{A}$,

$$\mathbf{J}_s \equiv \mathbf{J}_s[\psi,\mathbf{A}] = \frac{e_s\hbar}{2im_s}(\psi^*\nabla\psi-\psi\nabla\psi^*)-\frac{e_s^2}{m_s c}|\psi|^2\mathbf{A} = \frac{e_s}{m_s}|\psi|^2\left(\hbar\nabla\phi-\frac{e_s}{c}\mathbf{A}\right). \tag{3}$$

The quantity $|\psi|^2$ represents the local density of Cooper pairs (the superconducting charge carriers); $\hbar$ is Planck's constant divided by 2π; a and b are two positive constants; c is the speed of light; m_s and e_s are the effective mass and charge, respectively, of a Cooper pair; ν is the electrical conductivity; and D is the diffusion coefficient. As usual, i is the imaginary unit and an asterisk denotes complex conjugation. The *electric field* is $\mathbf{E}=(1/c)\partial_t\mathbf{A}+\nabla\Phi$, the *magnetic field* $\mathbf{B}=\nabla\times\mathbf{A}$.

The configurations used for the simulations model a superconducting core imbedded in a blanket of nonsuperconducting material (insulator or ordinary metal). No Cooper pair leaves the superconductor, so

$$\mathbf{n}\cdot\mathbf{J}_s=0 \tag{4}$$

at the interface between the superconductor and the blanket, where $\mathbf{n}$ is the local unit normal vector. Outside the superconductor, the order parameter is identically zero. Boundary conditions specify the magnetic field at the outer boundary.

The TDGL equations describe the gradient flow for the Ginzburg-Landau energy, which is the sum of the kinetic energy, the condensation energy, and the field energy,

$$E[\psi,\mathbf{A}]=\int\left[\frac{1}{2m_s}\left|\left(\frac{\hbar}{i}\nabla-\frac{e_s}{c}\mathbf{A}\right)\psi\right|^2+\left(-a|\psi|^2+\frac{b}{2}|\psi|^4\right)+|\nabla\times\mathbf{A}|^2\right]dx. \tag{5}$$

The integral extends over the entire configuration (superconductor plus blanket). An equilibrium configuration corresponds to a critical point of E.

The energy functional (5) assumes that there are no defects in the superconductor. Material defects can be naturally present or artifically induced and can be in the form of point, planar, or columnar defects (quenched disorder). A material defect weakens or eliminates the well in the condensation energy. This effect can be included in the Ginzburg-Landau model by making the parameter a position dependent and giving it a smaller value at the site of a defect.

Temperature is a parameter in the Ginzburg–Landau model; it features only in the coefficients a and b, and heat loss mechanisms are not accounted for. Thermal fluctuations can be included in a Langevin formulation, where a time-varying random source term is added to the equation for the order parameter. If the mean strength of the source term is zero, its standard deviation is a measure of temperature.

A. Dimensionless form

Let $\psi_\infty^2=a/b$, and let λ, ξ, and H_c denote the London penetration depth, the coherence length, and the thermodynamic critical field, respectively,

$$\lambda=\left(\frac{m_sc^2}{4\pi\psi_\infty^2e_s^2}\right)^{1/2},\quad \xi=\left(\frac{\hbar^2}{2m_sa}\right)^{1/2},\quad H_c=(4\pi a\psi_\infty^2)^{1/2}. \tag{6}$$

In this study, we render the TDGL equations dimensionless by measuring lengths in units of λ, time in units of the relaxation time ξ^2/D, fields in units of $H_c\sqrt{2}$, and energy densities in units of $(1/4\pi)H_c^2$. The nondimensional TDGL equations are

$$\left(\frac{\partial}{\partial t}+i\kappa\Phi\right)\psi=-\left(\frac{i}{\kappa}\nabla+\mathbf{A}\right)^2\psi+\psi-|\psi|^2\psi, \tag{7}$$

$$\sigma\left(\frac{\partial\mathbf{A}}{\partial t}+\nabla\Phi\right)=-\nabla\times\nabla\times\mathbf{A}+\mathbf{J}_s, \tag{8}$$

$$\mathbf{J}_s\equiv\mathbf{J}_s[\psi,\mathbf{A}]=\frac{1}{2i\kappa}(\psi^*\nabla\psi-\psi\nabla\psi^*)-|\psi|^2\mathbf{A}=|\psi|^2\left(\frac{1}{\kappa}\nabla\phi-\mathbf{A}\right). \tag{9}$$

The constant κ is the Ginzburg-Landau parameter $\kappa=\lambda/\xi$; σ is a dimensionless resistivity coefficient $\sigma=(4\pi\kappa^2D/c^2)\nu$. The interface condition (4) keeps the same form, although the symbols now stand for the corresponding dimensionless variables. The nondimensional TDGL equations are associated with the dimensionless energy functional

$$E[\psi,\mathbf{A}]=\int\left[\left|\left(\frac{i}{\kappa}\nabla-\mathbf{A}\right)\psi\right|^2+\left(-|\psi|^2+\frac{1}{2}|\psi|^4\right)+|\nabla\times\mathbf{A}|^2\right]dx. \tag{10}$$

In the system of dimensionless variables, the lower and upper critical field are $H_{c1}=(2\kappa)^{-1}(\ln\kappa+\frac{1}{2})$ and $H_{c2}=\kappa$, respectively. The thermodynamic critical field is $H_c=1/\sqrt{2}=0.707\ldots$, and the BCS depairing current is $j_{\mathrm{BCS}}=\frac{2}{9}\sqrt{3}=0.385\ldots$.[2]

When material defects are present, we replace the term $-|\psi|^2$ in the energy functional by $-\tau|\psi|^2$, where τ depends on position: $\tau(x)<1$ if x is in a defective region, $\tau(x)=1$ otherwise. The term ψ in Eq. (7) is then multiplied by the position-dependent factor τ.

We consider only rectangular geometries in a standard right-hand coordinate system: x from left to right, y from front to back, and z from bottom to top. The magnetic field is always oriented in the z direction.

B. Gauge choice and link variables

The (nondimensional) TDGL equations are invariant under a gauge transformation

$$\mathcal{G}_\chi:(\psi,\mathbf{A},\Phi)\mapsto(\psi e^{i\kappa\chi},\mathbf{A}+\nabla\chi,\Phi-\partial_t\chi). \tag{11}$$

We maintain the *zero-electric potential gauge*, $\Phi=0$, at all times using the link vector $\mathbf{U}$,

$$\mathbf{U}=e^{-i\kappa\int\mathbf{A}}. \tag{12}$$

This definition is componentwise, $U_x=e^{-i\kappa\int^x A_x(x',y,z)\,dx'}$, and so forth; U_x, U_y, and U_z are the *link variables* of lattice gauge theory.[3] The TDGL equations assume the form

$$\frac{\partial\psi}{\partial t}=-\frac{1}{\kappa^2}\sum_{\mu=x,y,z}U_\mu^*\frac{\partial^2}{\partial\mu^2}(U_\mu\psi)+\psi-|\psi|^2\psi, \tag{13}$$

$$\sigma\frac{\partial\mathbf{A}}{\partial t}=-\nabla\times\nabla\times\mathbf{A}+\mathbf{J}_s, \tag{14}$$

$$J_{s,\mu}\equiv J_{s,\mu}[\psi,U_\mu]=\frac{1}{\kappa}\mathrm{Im}\left[(U_\mu\psi)^*\frac{\partial}{\partial\mu}(U_\mu\psi)\right],\quad \mu=x,y,z. \tag{15}$$

C. Computational procedures

For the numerical solution of Eqs. (13)–(15), we evaluate ψ at the grid vertices (x_i,y_j,z_k) and A_x, A_y, and A_z at the midpoints $(x_i+\frac{1}{2}h_x,y_j,z_k)$, $(x_i,y_j+\frac{1}{2}h_y,z_k)$, and $(x_i,y_j,z_k+\frac{1}{2}h_z)$, respectively, of the edges of the computational grid. The supercurrent $\mathbf{J}_s$ and the link vector are evaluated at the same points as $\mathbf{A}$, while the magnetic field $\mathbf{B}$ is evaluated at the center $(x_i+\frac{1}{2}h_x,y_j+\frac{1}{2}h_y,z_k+\frac{1}{2}h_z)$ of each

grid cell. This placement of the evaluation points is dictated by the curl operator. The approximation is second-order accurate in space. Updating in time is done with a single-step forward Euler method.[4]

The TDGL code has been implemented on the IBM SP system at Argonne National Laboratory. At the time of the simulations, this system had 128 processors and 128 Mbytes per processor; most simulations were done using 16 processors. The transformations necessary to achieve parallelism are described elsewhere.[5] The code uses the message passing interface (MPI) standard[6] as implemented in the MPICH software library[7] to handle domain decomposition, interprocessor communication, and file I/O.

A simulation is normally initiated from the Meissner state. The TDGL equations are integrated through the transient state, and the simulations are continued into the steady state for as long as necessary to collect data for visualization and postprocessing analysis. Transport-driven systems exhibit fluctuations during the steady state, not only on the microscopic scale but also on the macroscopic scale, so in practice it is often difficult to say when exactly a steady state has been reached. We adopt a pragmatic point of view and allow for some fluctuations of macroscopic quantities within narrowly defined limits (for example, a variation of less than 1% in the numnber of vortices). We note that a very large number of time steps is sometimes needed to reach steady state.

Both two- and three-dimensional configurations are used. Two-dimensional configurations are cross sections of three-dimensional configurations that are infinite and homogeneous in the direction of the field (i.e., the z direction). We assume periodicity in the y direction. We have $\mathbf{A}=(A_x,A_y,0)$, $\mathbf{J}_s=(J_{s,x},J_{s,y},0)$, and $\mathbf{B}=(0,0,B)$, with $B=\partial_x A_y-\partial_y A_x$. The boundary conditions specify the magnetic field $B=B_L$ at the left surface, $B=B_R$ at the right surface; $B_L=B_R$ if the field is uniform. A nonzero differential B_L-B_R generates a bulk transport current in the y direction. The periodicity condition implies that we model a segment of a current path, rather than a current loop, so we avoid edge effects. A transport current in the y direction acting on a vortex (magnetic flux tube) oriented in the z direction results in a Lorentz force in the x direction, $\mathbf{F}=(F,0,0)$. In three-dimensional simulations we have the option of imposing a transport current in the x or y direction.

In a two-dimensional system, each vortex is a straight line parallel to the z axis. Its position in the (x,y) plane is found by integrating the supercurrent $\mathbf{J}_s$ once around the circumference of a computational mesh cell: a measurable value of the integral indicates the presence of a vortex in the interior of the cell. (The presence of more than one vortex is excluded if the computational grid is sufficiently fine. In our simulations, a computational mesh cell measures two coherence lengths along each side.) Having found the position of each vortex, we generally use a Delauney triangulation to analyze the structure of the vortex lattice. Each vortex in the bulk with fewer or more than six neighbors identifies a defect in the lattice.

Finding vortices in three dimensions is not trivial. In principle, one can find the point of intersection of a vortex with each transverse plane and connect these points in the longitudinal direction to generate the vortex lines. In practice, it is difficult to design a procedure that consistently makes the correct connections, especially when the vortices are moving. For this reason, we rely mostly on visualization techniques, drawing isosurfaces of $|\psi|$ and $B=|\nabla\times\mathbf{A}|$.

Much relevant information about the properties of a superconductor is obtained by measuring the voltage response to a driving current. The voltage difference between two leads is proportional to the average velocity of the vortices crossing the line joining the leads. In the simulations, we compute the voltage difference between two points by integrating the electric field along the line joining the two points.

III. DRIVEN VORTEX SYSTEMS

In this section we present the results of several simulations of vortex motion in the presence of a twin boundary (Sec. III A), point defects in two dimensions (Sec. III B), and columnar defects in three dimensions (Sec. III C).

A. Twin boundary effects

Twin boundaries in YBCO provide a prototypical example of strong anisotropic pinning by an extended defect.[8] While initial magneto-optical experiments[9] showed that twin boundaries are planes of reduced pinning, allowing flux to penetrate more deeply into the superconductor than in the surrounding untwinned regions of the crystal, later studies[10] found twin boudaries to be barriers to flux penetration. The apparent conflict was resolved by further magneto-optical experiments,[11] which revealed that the nature of the twin boundary pinning depends on the direction of the Lorentz force driving the vortex motion. Barrier action occurs when the Lorentz force is perpendicular to the twin boundary, while deep penetration occurs when the Lorentz force is parallel to the twin boundary.

The purpose of the first set of simulations is to explore the interplay between pinning and driving forces in more detail. We find that, at weak driving currents, a twin boundary dominates both the local structure and the motion of vortices. The twin boundary is an impenetrable barrier to vortex motion, and in the bulk the vortex system shows plastic motion. As the current increases, the vortices in the twin boundary are no longer stationary, there is motion in the twin boundary, and vortices may cross the twin boundary at weak spots. At strong currents, the driven vortex system behaves like an elastic medium, and most trajectories suffer only a slight perturbation at the twin boundary.

The configuration used for these simulations is that of a superconductor (GL parameter $\kappa=4$) that is infinite and homogeneous in the direction of the field (z), periodic in y, and bounded in x. The (x,y) cross section measures $32\lambda\times48\lambda$. The superconductor is embedded in an insulating layer (air), which is $\frac{1}{4}\lambda$ thick. A driving current in the y direction is generated in the bulk by a field differential between the left and right boundary,

$$B_L=0.8+K,\quad B_R=0.8-K, \tag{16}$$

K is variable (units of $H_{c\sqrt{}}2$). The twin boundary is modeled as a ''trench'' running from left to right at a 45° angle, two correlation lengths wide, where the condensation energy is reduced randomly to a mean value of 56% of the bulk value

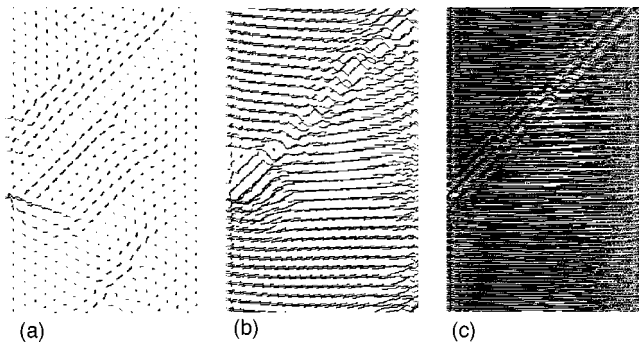

FIG. 1. Vortex trajectories in the presence of a twin boundary.

and normally distributed with a standard deviation of 25%. Outside the twin boundary, the bulk of the sample is free of defects.

Figure 1 shows the vortex trajectories at increasingly stronger driving currents. We discuss each case in detail.

Weak Current [Fig. 1(a)]. The twin boundary dominates both the local structure and the motion of vortices. The vortices in the twin boundary are stationary, being pinned against motion by the random potential; the twin boundary is an impenetrable barrier to vortex motion; vortex motion in the bulk is plastic motion, and the direction of motion of the vortices is primarily along the close-packed directions of the lattice.

The last feature especially explains the guided motion that occurs in Fig. 1(a): The twin boundary defines the close-packed directions, this orientational order persists over long range (up to the dimension of the simulated sample), and vortex motion is restricted to the close-packed directions. As a result, the twin boundary determines the velocity direction of vortices even at distant points.

A characteristic feature of Fig. 1(a) is the occurrence of velocity discontinuities—most obviously at the twin boundary, where the velocity suddenly jumps from zero to approximately its highest value in one lattice spacing. This is quite different from the hydrodynamic motion of liquids, where the velocity profile grows monotonically from zero at the boundary, reaching its highest value deep in the liquid. Additional discontinuities occur far from any local structural feature. Four rows above the twin boundary, the velocity abruptly jumps from a high value to nearly zero, and there are discontinuous velocity changes two rows and seven rows below the boundary. Farther below the twin boundary, after a region of little or no motion, two adjacent rows of vortices suddenly flow at substantial velocity parallel to the twin boundary. The discontinuities associated with these two rows have no apparent communication with the twin boundary or with the guided motion adjacent to the boundary. They illustrate the collective nature of the plastic response of the vortices to the particular driving and pinning forces in the simulation.

The plastic motion in Fig. 1(a) displays discontinuities in the direction as well as the magnitude of the vortex velocity. Near the left edge of the sample, just below the twin boundary, there are several rows of vortices moving to the lower right with substantial speed. These vortices border on another group moving to the upper right with approximately equal speed. The discontinuity in direction is dramatic: the velocity change occurs in one vortex spacing with no transition region. This velocity direction discontinuity may be understood in terms of the principle of motion restricted to close-packed directions. The lattice accommodates the twin boundary by orienting one of its close-packed directions along the boundary, as described above. Since the twin boundary is a barrier to vortex flow, the other two close-packed directions are effectively blocked as paths for motion. If any motion is to occur, it must be along the close-packed direction parallel to the twin boundary. However, just below the left end of the twin boundary, the barrier effect is absent, and all close-packed directions are available for vortex motion. The vortices choose to move to the lower right, because it is the close-packed direction oriented nearest to the direction of the Lorentz force.

Despite the velocity discontinuities, there is a great deal of correlation in the vortex motion in Fig. 1(a). The four rows of vortices above the twin boundary move with approximately equal average velocity, as do the two rows just below the boundary and the fifth to seventh rows below. These correlations of neighboring velocities are easy to understand qualitatively as an effect of the shear modulus. Elastic energy is minimized if neighboring vortices move at the same velocity, so that the shear bonds are not stretched. In spite of this mechanism, the velocity correlations are relatively short range, extending less far than the orientational correlation of the lattice.

Intermediate current [Fig. 1(b)]. The driving force has become comparable with the twin boundary pinning forces, and the twin boundary no longer dominates the motion of vortices. The vortices in the twin boundary are no longer stationary; there are crossing trajectories in the twin boundary; vortex motion in the bulk is beginning to resemble elastic motion; and the direction of motion of the vortices is determined primarily by the Lorentz force.

In fact, a new kind of guidance occurs, where vortices move parallel to the boundary but internal to it.[12] This internal guidance is most easily seen at the lower left of the twin boundary, but it also occurs elsewhere along the boundary over shorter distances in regions where the random pinning wells are relatively deep compared with the bulk but still comparable in depth to neighboring wells. The driving force is sufficient to overcome the relatively low local barriers between wells, but insufficient to overcome the larger barriers blocking access to the bulk.

The high correlation among vortex trajectories near the twin boundary, which was apparent at the weaker current, is missing. The fact that some vortex trajectories cross the twin boundary indicates that different vortices do not necessarily follow the same path when encountering the same pinning configuration at different times. Their motion depends not only on the pinning configuration, but also on the local vortex configuration at the time of the encounter.

The twin boundary, which has lost its structure, no longer appears as an extended object to the vortices. Rather, it is a line of random pinning wells, some of which are strong enough to trap vortices. Without local structure, there are no well-defined close-packed directions and no structural features to guide the motion of vortices. The randomness associated with the relative sizes of the pinning and Lorentz forces at this current destroys the coherence of the boundary and is ultimately responsible for the disorder that character-

izes the plastic motion in Fig. 1(b). Where there is no random element, as in the bulk of the sample, the motion is highly ordered.

Far from the twin boundary, where pinning is absent, a new order appears in the vortex motion. Figure 1(b) shows a remarkable uniformity in the vortex trajectories. The vortices all move in nearly the same direction with the same speed. Further, the direction of motion is nearly the Lorentz force direction, not the twin boundary direction. The motion of Fig. 1(b) is the beginning of elastic motion, where all vortices move with the same average velocity. The effect of the twin boundary on the vortex velocities is greatly reduced. There is only local influence in the vicinity of the twin boundary, and it upsets the elastic order imposed by the Lorentz force, rather than defining the orientational order that controls the Lorentz force. At this driving current, we clearly see a competition between the Lorentz force and the pinning forces. Neither is dominant, and the unstructured velocities of the vortices near the twin boundary reflect the incoherent nature of their response.

Strong current [Fig. 1(c)]. The Lorentz force clearly overwhelms the twin boundary pinning forces, and the motion is elastic everywhere. Most trajectories suffer only a slight perturbation at the twin boundary.

B. Point defects

The TDGL equations enable a close look at vortex motion through arrays of point defects. The numerical simulations in this section show the actual effect of two regular defect arrangements—one with rectangular symmetry, the other with triangular symmetry—on the number of vortices, the vortex trajectories, and the magnetic field in a superconductor.

The simulations lead to a number of observations. The triangular defect arrangement accommodates more vortices (at steady state) than the rectangular defect arrangement and is slightly more effective at vortex pinning, at least at weak driving currents. Vortices travel along well-established tracks, which are formed early in the transient phase. The average vortex spacing increases in the direction of vortex motion and enforces the formation of fault lines in the lattice structure of the moving vortices. When the driving force is weak, the magnetic field is determined primarily by the vortices that are pinned on the defects, and vortex motion in the transverse direction has a smoothing effect on the magnetic field.

The basic configuration used for these simulations is two dimensional: a superconductor measuring $33\lambda \times 48\lambda$, periodic in y, embedded in a thin insulating blanket ($\frac{1}{4}\lambda$). A bulk transport current is generated in the y direction by a field differential between the left and right surface,

$$B_L = 2H, \quad B_R = 0. \tag{17}$$

H is thus the average applied field, which is variable.

A total of 160 point defects are arranged regularly in the interior in 16 rows and 10 columns. The columns are 3λ apart, so a defect-free zone of 3λ is left adjacent to the left and right surface. A defect covers one computational mesh cell (which is one-half coherence length on each side), so the density of the defects is 0.16%. All defects have the same strength; the condensation energy at each defect is 56% of the bulk value. In the arrangement with rectangular symmetry, the defects are placed in a regular square pattern; in the arrangement with triangular symmetry, every other column is shifted vertically over a distance 1.5λ.

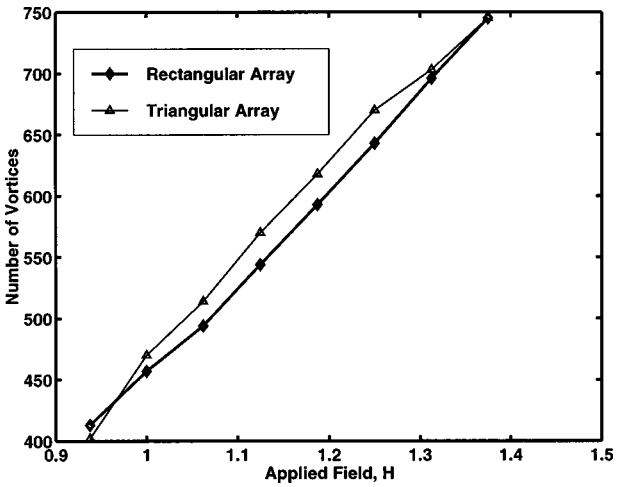

FIG. 2. Number of vortices at steady state as a function of the applied field.

We note that it takes considerable time to reach the steady state, especially when the defects are arranged in a triangular pattern and when the bulk transport current is weak.

Figure 2 illustrates the observation that the triangular defect arrangement accommodates more vortices than the rectangular defect arrangement. The number of vortices in the system at steady state (including the 160 vortices that are pinned on the defects at all times) ranges from approximately 413 at $H=0.9375$ to 745 at $H=1.375$ and is generally higher for the triangular arrangement. The one exception, at the weakest current, indicates that the steady state was probably never reached in this case. The difference is small but measurable (approximately 5%), and becomes smaller as the driving force increases. At the strongest current considered here, the difference has disappeared altogether.

Figures 3 and 4 support the observation that the triangular defect array may be more effective at vortex pinning, at least at weak driving currents. Figure 3 shows the I-V curves deduced from the simulations ($I=2H$). The rectangular defect

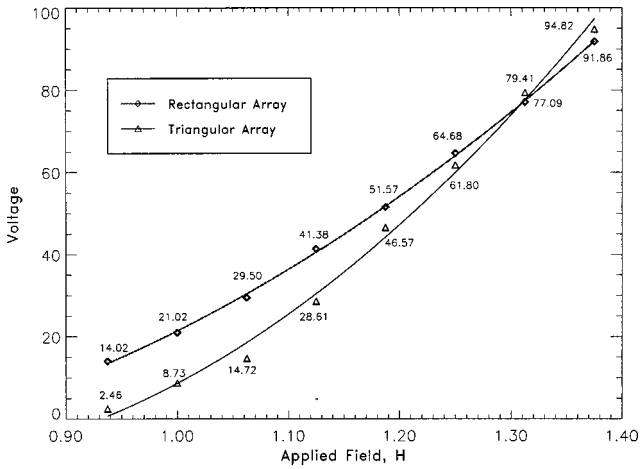

FIG. 3. Current ($I=2H$) vs voltage.

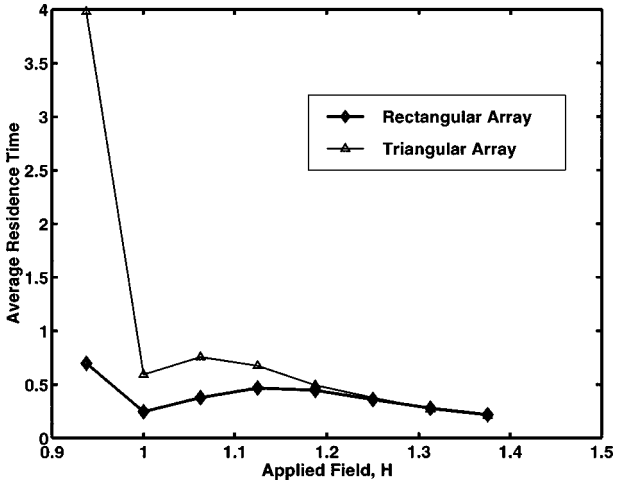

FIG. 4. Vortex residence time at steady state as a function of the applied field.

arrangement yields a higher voltage at low currents and a lower voltage at high currents; the crossover occurs around $H=1.3$, a little below the strongest driving force used in these simulations. Figure 4 shows the residence times, a measure of the average time spent by a vortex in the system as it moves across the sample (not counting vortices that are pinned). The triangular defect arrangement forces the vortices to spend more time in the system, certainly at weak currents. The difference becomes less pronounced as the driving force increases, and beyond some point the arrays appear equally effective.

The vortex trajectories are shown in Fig. 5 (rectangular defect arrangement) and Fig. 6 (triangular defect arrangement). Both cases show that the vortices tend to travel along well-established tracks—a phenomenon shown most graphically by Harada *et al.*[13] The track patterns are established during the transient phase and maintained in a very stable manner during the steady state.

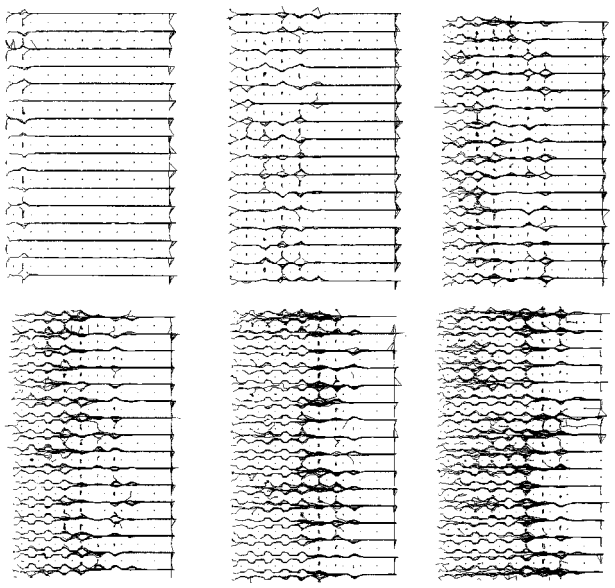

FIG. 5. Vortex trajectories through a rectangular array of point defects; top row, from left to right: $H=0.9375,\ 1.0625,\ 1.1875$; bottom row, from left to right: $H=1.250,\ 1.3125,\ 1.375$.

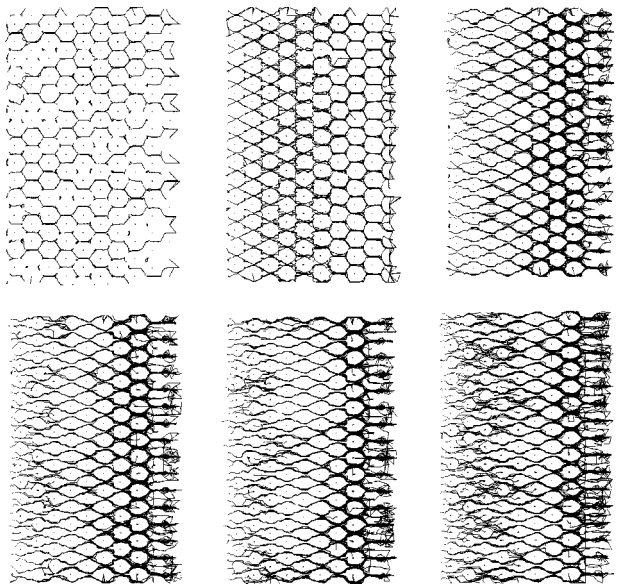

FIG. 6. Vortex trajectories through a triangular array of point defects; top row, from left to right: $H=0.9375,\ 1.0625,\ 1.1875$; bottom row, from left to right: $H=1.250,\ 1.3125,\ 1.375$.

Rectangular defect arrangement (Fig. 5). When the driving current is weakest, the tracks are straight and run midway between the defects. Deviations from this pattern occur near the left surface; for example, some vortices are being trapped at an interstitial site, while others that had been trapped earlier at an interstitial site manage to escape and travel down the nearest available straight-line track. The vortex pattern is highly regular; a triangulation of the moving vortex lattice shows that it is virtually free of defects.

As the average field (and, hence, also the driving current) increases, more vortices need to be accommodated, and multiple tracks develop between adjacent defects near the left surface, where the vortices enter. The straight-track pattern observed at weak current still exists but is pushed further into the interior. In the left zone, vortices are squeezed between vertically adjacent defects along two tracks in an alternating pattern, their passage being facilitated by a slight up-and-down motion of the vortices that are pinned at the interstitial sites. Gradually, as the vortices are driven to the right and accelerate, the tracks straighten out and merge to form the straight-line track pattern observed at the weakest current. Since the number of vortices flowing across the sample per unit time is constant, the increase in vortex velocity is accompanied by a corresponding decrease in vortex density. In fact, the density seems to change rather abruptly where the tracks merge. This rather abrupt change in the vortex density is associated with a fault line in the structure of the vortex lattice: Fault lines provide a mechanism to accommodate strains resulting from an increase in the intervortex spacing.[14]

The up-and-down motion of the vortices that are pinned at the interstitial sites (mentioned in the preceding paragraph) can be observed directly. But there is also indirect evidence. Figure 7 shows the temporal evolution of the voltage drop between two leads placed, respectively, at 2.5λ from the left surface, at the center of the sample, and at 2.5λ from the right surface ($H=1.375$). During an initial transient, which starts successively at the left-most, center, and right-most

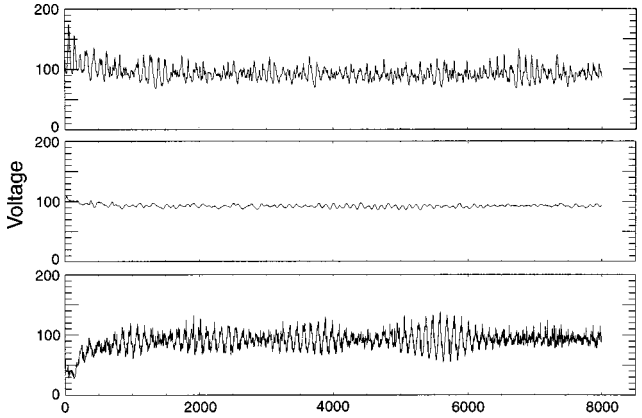

FIG. 7. Temporal evolution of the voltage drop along a vertical line at 2.5λ from the left surface (top), in the center of the sample (middle), and at 2.5λ from the right surface (bottom). The width of the superconductor is 33λ. ($H=1.375$.)

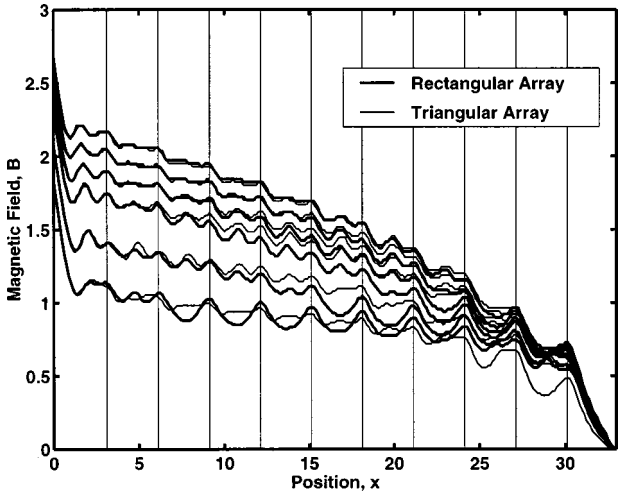

FIG. 8. Magnetic field across the sample (averaged over y). From bottom to top: $H=0.9375$, 1.0625, 1.1875, 1.250, 1.3125, 1.375. Vertical lines mark the positions of the defects.

position, the voltage rises to some nonzero average value. Once the steady state is reached, each voltage keeps oscillating, and the oscillations are clearly modulated. The oscillations mark the passage of individual vortices across the line joining the leads. They are stronger near the surfaces, and their average frequency is determined by the vortex velocity and density. The modulations are manifestations of the up-and-down motion of the vortices that are pinned at the interstitial sites; as they move, they exert an accelerating or decelerating influence on the velocity of each passing vortex.

Triangular defect arrangement (Fig. 6). Especially at the weakest current, many vortices are again pinned at interstitial sites in the bulk. They force approaching vortices into a northeastern or southeastern direction and create the open loops in the hexagonal track pattern. A triangulation of the positions of the moving vortices shows a lattice structure with a fair number of defects, but no discernible patterns.

As the average field increases and more vortices need to be accommodated, the hexagonal pattern near the left surface is replaced by a quadrilateral (diamond) pattern. The hexagonal pattern still persists, but further into the interior. The transition occurs in one or at most two column widths. This transition zone separates a high-density region on the left from a low-density region on the right. Again, a decrease in density is accompanied by a corresponding increase in velocity, so the flux remains constant. As more vortices must be accommodated, vertical motion of the vortices becomes more difficult near the left surface. The diamonds open up, and the tracks become more clearly separated.

Figure 8 shows the magnetic field B, across the superconductor for various values of H. The thick curves correspond to the rectangular defect arrangement, the thin curves to the triangular defect arrangement. When the driving force is weak (bottom curves), the magnetic field is determined primarily by the vortices that are pinned on the defects, and the maxima coincide with the x positions of the defects. The maxima are less pronounced when the defects are arranged in a triangular pattern than when they are arranged in a rectangular pattern. The smoothing is a result of vortex motion in the transverse (y) direction; in the rectangular arrangement such motion is virtually absent, while it is relatively significant in the triangular arrangement (see Figs. 5 and 6). As the driving force increases (middle curves), motion in the y direction becomes more significant, both with the rectangular and the triangular defect arrangement. The field still shows some oscillatory behavior, but the oscillations are less pronounced. The field appears to be slightly stronger in the triangular case. At the strongest driving force (top curves), the difference between the two arrangements has virtually disappeared. The field is determined by the moving vortices, and in both cases there is enough motion in the y direction that the field profile is almost flat between adjacent defect columns.

Several of the findings outlined above have been confirmed in other simulations. For example, we observe channel motion in a large superconductor ($120\lambda \times 48\lambda$) with randomly placed point defects. While some vortices are pinned on the defects, others move through meandering tracks passing between the point defects. The channels form during the transient phase and remain remarkably stable. Their shape is irregular because of the random placement of the defects. After introducing thermal noise, we still observe channel motion, but the phenomenon is considerably obscured by the fluctuations in the vortex trajectories. Also, the motion evolves on a different time scale and is more akin to creep motion.

C. Columnar defects

In this section we present the results of some three-dimensional simulations. Simulations of this type are extremely time consuming, and systematic parameter studies are still prohibitively expensive. We focus on vortex motion through columnar defects. Columnar defects, which are introduced in a superconducting crystal by irradiation with heavy ions, increase the critical current, extend the irreversible region, and impede vortex creep motion.[15] Splaying the columnar defects with respect to the magnetic field has been proposed as a mechanism to further enhance the transport properties.[16] Our simulations show that, under certain conditions, splaying can have the opposite effect, as it facilitates a kinking-induced transfer of a vortex from one defect to another.

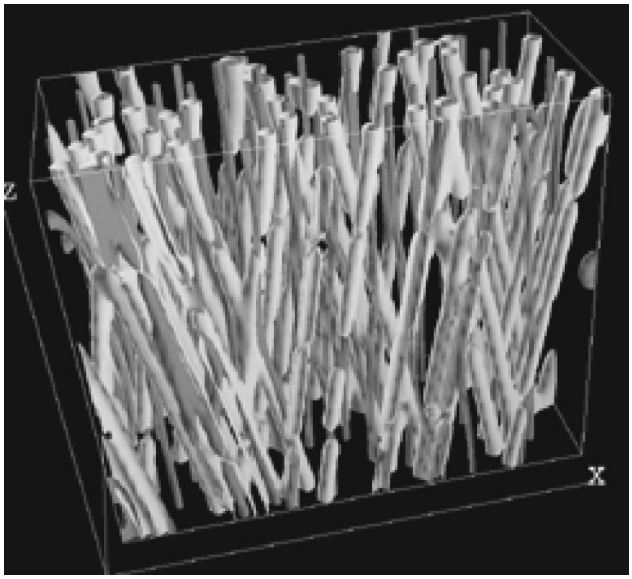

FIG. 9. Vortex motion through splayed columnar defects.

The configuration used for these simulations consists of a superconductor measuring $14\lambda \times 6\lambda \times 12\lambda$, periodic in y, embedded in an insulating blanket (thickness $\frac{1}{2}\lambda$). A bulk transport current in the y direction generates a driving force in the x direction.

Splayed columnar defects are introduced as follows. First, the bottom plane surface of the superconductor is seeded randomly with point defects of variable strength (density 1%). Next, the point defects are extended upward into the interior of the superconductor to generate vertical columnar defects parallel to the applied field. The columns are subsequently tilted (splayed) at an angle of $\pm 10°$ with respect to the applied field, either in the (x,z) plane or in the (y,z) plane. The positive and negative tilting directions are chosen randomly from a uniform distribution, in such a way that approximately one-half of all columns is tilted one way and approximately one-half the other. This type of configuration is referred to as ''splayed.'' By splaying the columns in the (x,z) plane, we simulate ''in-fan'' vortex motion (i.e., motion in the tilt plane); by splaying the columns in the (y,z) plane, we simulate ''across-fan'' vortex motion (i.e., motion transverse to the tilt plane). In the latter configuration, the vortices see the defects as V-shaped obstacles. Figure 9 gives a typical snapshot of ''in-fan'' motion. The lighter objects are the defects: they are stiff and stationary; the darker objects are the vortices: they are flexible and move. (The defects are really straight; the pinched structure is due to an error in the visualization code.) The strength of the magnetic field is chosen so the number of vortices is approximately equal to the number of defects (''matching field'').

The observation that splaying the columnar defects actually enhances vortex motion is supported by the voltage curves of Fig. 10. The four curves show the temporal evolution of the voltage in four cases: (a) in-fan vortex motion through splayed columnar defects, (b) across-fan vortex motion through splayed columnar defects, (c) columnar defects parallel to the field, same defect seeding as for (a), and (d) columnar defects parallel to the field, same defect seeding as for (b). The voltages vary somewhat with time—an indication that we have not reached steady state yet—but eventually both splayed configurations yield a higher voltage than either of the parallel configurations. A higher voltage represents greater vortex velocities.

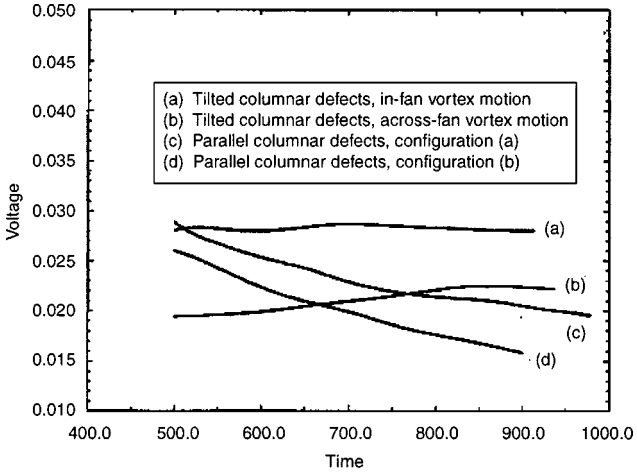

FIG. 10. Vortex motion through columnar defects. Voltage vs time.

The observation may seem counterintuitive at first, but can be explained by the mechanism of kinking-induced vortex transfer. Given the strength of the defects, the vortices prefer to be pinned to a defect. If the columns are parallel to the field, the vortices are pinned over their entire length, and it takes considerable energy to drive them off a defect. If the columns are splayed, a small kink in the vortex is sufficient to initiate a transfer to the next available defect.

The sequence of snapshots of Fig. 11 captures the kinking-induced transfer of a vortex from one defect to another. The defects are the thin straw-like objects, the vortices the darker flexible tubes. A vortex that is originally pinned on a defect develops a loop in the interior of the sample; the loop peels off and is pulled to the next defect. The loop extends in both directions in a travelling-wave-like scenario, and gradually the entire vortex transfers to the next available defect.

IV. TRANSITION TO THE VORTEX STATE

How vortices are formed as a superconductor enters the vortex state from the Meissner state is a topic of considerable

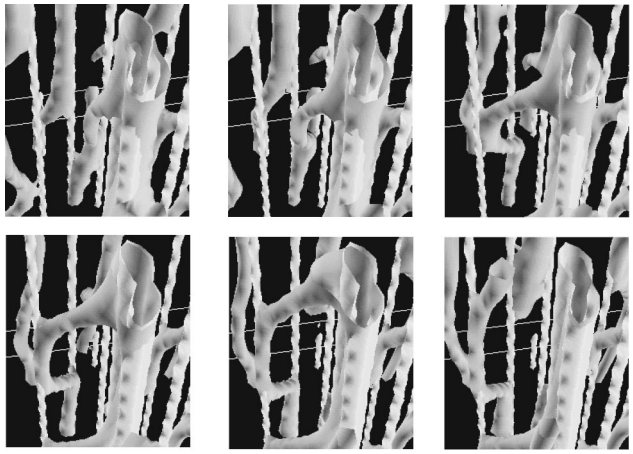

FIG. 11. Kinking induced motion of vortices through splayed columnar defects.

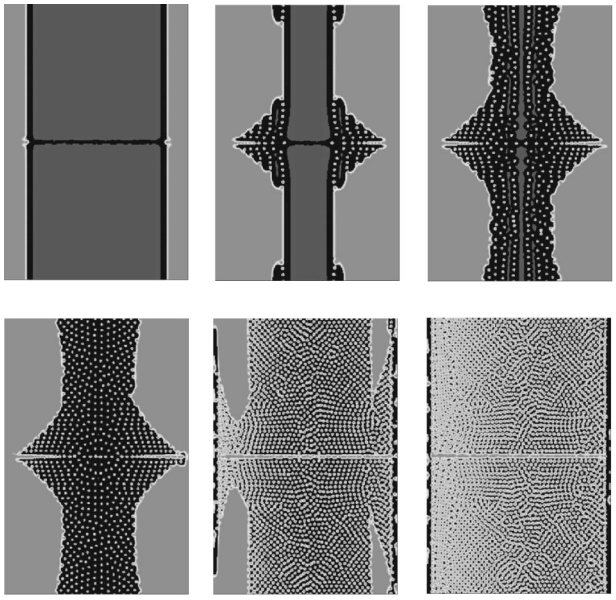

FIG. 12. Vortex deposition in two dimensions.

debate and uncertainty. The time scales are too short for experimental observations, although some exploding-coil experiments have been reported recently in the literature.[17] Typically, in these experiments the field is ramped up to several hundred T in a few ms. The TDGL equations offer a unique tool to explore the transition to the vortex state, and in this section we summarize the results of several numerical simulations based on the TDGL equations.

Simulations in two- and three-dimensional systems support a scenario where vortices are formed in the bulk of the sample through a process of ''deposition.'' As the ambient field ramps up, it rushes into the superconductor. The front becomes unstable, its curvature increases, and vortices are spawned. The process is illustrated in Figs. 12 and 13. The time scale on which the evolution represented in these figures proceeds is difficult to estimate because the time has been nondimensionalized by means of the unknown diffusion coefficient. Our best guess is that the entire deposition scenario evolves in a matter of microseconds.

Vortex deposition in two dimensions. Figure 12 gives a series of snapshots of $|\psi|$ taken during the transient phase; dark gray corresponds to a value close to 1 (Meissner state), light gray to a value close to 0 (normal state), and vortices are set off against a black background. The configuration measures $32\lambda \times 48\lambda$ and is periodic in y. A twin boundary (planar defect, two coherence lengths wide) extends from left to right, perpendicular to the lateral surfaces. The system is originally in the Meissner state; at $t=0$, the field is raised, $B_L=0.82$, $B_R=0.78$. (The very small bulk transport current helps to drive the vortex system to steady state.)

At the start of the computation, the system is almost entirely in the Meissner state (dark gray); the order parameter is slightly depressed near the left and right surface and the planar defect. Raising the applied magnetic field results almost immediately in a suppression of the order parameter in a fairly large region near the lateral surfaces. (The slight asymmetry is a result of the transport current.) As the fronts of the suppressed regions approach each other, they became unstable, especially near the planar defect. The instabilities develop into vortices, and the fronts assume complicated spatial structures. The formation of vortices continues, with a concomitant rapid reduction of the free energy. At the same time, the fronts of the suppressed regions retreat toward the boundaries, but the order parameter remains suppressed in the region of the defect. The planar defect facilitates the formation of vortices, and soon the vortex region extends all the way across the sample. Eventually, the entire superconductor is in the vortex state; the highest vortex density is found in the twin boundary. The total number of vortices in the system is approximately 2700.

Once the vortex state has been reached, the remainder of the transient is spent on a rearrangement of the vortex configuration, with a gradual decrease of the free energy. In the absence of any driving forces, this rearrangement proceeds very slowly. A detailed investigation of the structure of the vortex lattice reveals that the system evolves toward a more perfect lattice. The orientation of the lattice and the location and nature of the remaining lattice defects depend on the relative importance of the pinning forces due to the surfaces and the planar defect.[14]

Vortex deposition in three dimensions. Figure 13 gives a series of snapshots of two isosurfaces of the magnetic field during the transient phase of a transition from the Meissner state to the vortex state in a three-dimensional system. The configuration consists of a homogeneous superconducting strip (periodic in y, measuring $8\lambda \times 2\lambda$ in the (x,z) plane, no defects) imbedded in a normal metal. The computational domain, including the metal blanket, measures $14\lambda \times 2.5\lambda \times 12\lambda$, with periodicity in the y direction. A uniform magnetic field (in the z direction) with $B_L=B_R=2.8$ is applied at $t=0$. We follow the evolution of the system to the vortex state by monitoring the magnetic field.

The figure shows how the magnetic field first penetrates the superconducting strip and then retreats as flux tubes are spawned in the interior of the strip. The scenario of vortex deposition is similar to the one observed above in two dimensions. Because there are no defects in the system, the final arrangement of the flux tubes is perfectly symmetric.

When thermal fluctuations are included, the scenario is basically the same but proceeds in a much more irregular fashion. Isosurfaces seem to float and coalesce in the strip, and flux tubes form more or less by condensation of fluctuations. Figure 14 shows a typical vortex configuration.

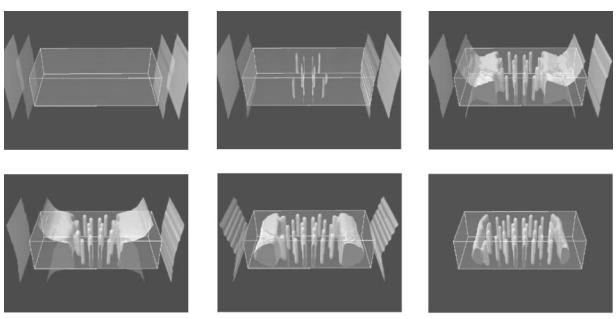

FIG. 13. Vortex deposition in three dimensions.

V. SUMMARY AND DISCUSSION

In this article we have presented the results of several large-scale numerical simulations of vortex motion in super-

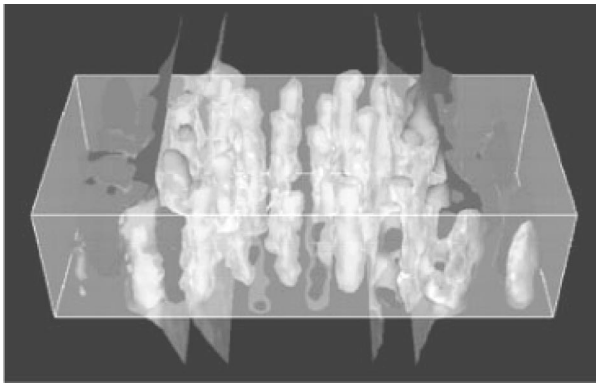

FIG. 14. Vortex configuration in the presence of thermal fluctuations.

conducting media. The simulations are based on the TDGL equations of superconductivity and give the best results currently obtainable on a macroscopic scale without *a priori* assumptions about the number of vortices or the nature of the interactive forces among the vortices.

The simulations shed considerable light on collective vortex motion in the presence of quenched disorder, showing guided motion in the presence of a twin boundary, channel motion in the presence of point defects, and kinking-induced motion through columnar defects. The simulations show that vortex motion in the presence of a twin boundary may be plastic or elastic, depending on the relative strength of the pinning and driving forces. From the details of trajectories it is possible to make qualitative judgments as to the relative merits of certain defect arrangements. In particular, the simulations show that a triangular arrangement of point defects may be better at pinning vortices than a rectangular arrangement and that splaying columnar defects with respect to the magnetic field has the effect of actually enhancing the average vortex velocity. The simulations also provide insight in the process of vortex formation, showing that the process evolves via a scenario of vortex deposition in the bulk.

Simulations based on the TDGL equations are extremely time consuming and require significant computing resources. They are therefore more useful for qualitative than for quantitative studies. For example, they can give information about the dynamic phases of a driven vortex system, but not about the exact location of the transition lines. Systematic parameter studies are still prohibitively expensive.

ACKNOWLEDGMENTS

The work was supported by the Mathematical, Information, and Computational Sciences Division subprogram of Advanced Scientific Computing Research (D.G., H.K., G.L.) and the Materials Science Office of the Basic Energy Sciences program (G.C., A.K., V.V.) of the U.S. Department of Energy under Contract No. W-31-109-Eng-38.

[1] V. L. Ginzburg and L. D. Landau, Zh. Eksp. Teor. Fiz. **20**, 1064 (1950); D. ter Haar, *L. D. Landau; Men of Physics* (Pergamon, Oxford, 1965), Vol. I, pp. 138–167; A. Schmid, Phys. Kondens. Mater. **5**, 302 (1966); L. P. Gor'kov and G. M. Eliashberg, Zh. Eksp. Teor. Fiz. **54**, 612 (1968) [Sov. Phys. JETP **27**, 328 (1968)].

[2] M. Tinkham, *Introduction to Superconductivity*, 2nd ed., (McGraw-Hill, New York, 1996), Eq. (4.36).

[3] J. B. Kogut, Rev. Mod. Phys. **51**, 659 (1979); **55**, 775 (1983).

[4] W. D. Gropp *et al.*, J. Comput. Phys. **123**, 254 (1996).

[5] N. Galbreath *et al.*, *Proceedings of the Sixth SIAM Conference on Parallel Processing for Scientific Computing*, edited by R. F. Sincovec *et al.* (SIAM, Philadelphia, 1993), pp. 160–164.

[6] J. Dongarra *et al.*, *MPI–The Complete Reference* (MIT Press, Cambridge, MA, 1998), Vols. I and II.

[7] W. Gropp, E. Lusk, and A. Skjellum (unpublished).

[8] G. W. Crabtree *et al.*, Phys. Rev. B **36**, 4021 (1987); W. K. Kwok *et al.*, Phys. Rev. Lett. **64**, 966 (1990); E. M. Gyorgy *et al.*, Appl. Phys. Lett. **56**, 2465 (1990); L. Ya. Vinnikov *et al.*, Pis'ma Zh. Éksp. Teor. Fiz. **47** 109 (1988) [JETP Lett. **47**, 131 (1988)]; Solid State Commun. **67**, 421 (1988); G. J. Dolan *et al.*, Phys. Rev. Lett. **62**, 827 (1989); L. J. Swartzendruber *et al.*, *ibid.* **64**, 483 (1990); U. Welp *et al.*, Appl. Phys. Lett. **57**, 84 (1990).

[9] C. A. Duran *et al.*, Nature (London) **357**, 474 (1990); M. Turchinskaya *et al.*, Physica C **216**, 205 (1990).

[10] V. K. Vlasko-Vlasov *et al.*, Phys. Rev. Lett. **72**, 3246 (1994).

[11] U. Welp *et al.*, Physica C **241**, 235 (1994); C. A. Duran *et al.*, Phys. Rev. Lett. **74**, 3712 (1995); U. Welp *et al.*, *ibid.* **74**, 3713 (1995).

[12] G. W. Crabtree *et al.*, Physica C **263**, 401 (1996).

[13] K. Harada *et al.*, Science **274**, 1167 (1996).

[14] D. W. Braun *et al.*, Phys. Rev. Lett. **76**, 831 (1996).

[15] L. Civale *et al.*, Phys. Rev. Lett. **67**, 648 (1991); M. Konzcykowski *et al.*, Phys. Rev. B **44**, 7167 (1991); D. R. Nelson and V. M. Vinokur, Phys. Rev. Lett. **68**, 2398 (1992); Phys. Rev. B **48**, 13 060 (1993).

[16] T. Hwa *et al.*, Phys. Rev. Lett. **71**, 3545 (1993); L. Krusin-Elbaum *et al.*, *ibid.* **76**, 2563 (1996); D. Lopez *et al.*, *ibid.* **79**, 4258 (1997); W. K. Kwok *et al.*, *ibid.* **80**, 600 (1998).

[17] A. S. Dzurak *et al.*, Phys. Rev. B **57**, R14 084 (1998); H. Nakagawa *et al.*, Physica B **246-247**, 429 (1998).